Is the storm time response of the inner magnetospheric hot ions universally similar or driver dependent?

Michael W. Liemohn[1] and Roxanne Katus[1]

Received 18 November 2011; revised 23 February 2012; accepted 24 February 2012; published 7 April 2012.

[1] The Hot Electron and Ion Drift Integrator (HEIDI) model was used to simulate all of the intense storms ($Dst_{min} < -100$ nT) from solar cycle 23 (1996–2005). These storms were classified according to their heliospheric driving structure, namely, either an interplanetary coronal mass ejection (ICME) or a corotating interaction region and its trailing high-speed stream (CIR/HSS). Five different HEIDI input combinations were used to create a large collection of numerical results, varying the plasma outer boundary condition and electric field description in the model. Statistical data-model analyses were conducted on the total energy content, yielding error estimates on the correlation coefficients and root-mean-square error values for each run set. The accuracy of each run set depends on the method of comparison and classification of the driver. For the correlation coefficients, the simulations using a local-time-dependent outer boundary condition were consistently better than those using a local-time-averaged (but high-time-resolution) nightside boundary condition, with the simplistic electric field being better than the self-consistent field description. For the root-mean-square error, the results are less conclusive. For the CIR/HSS-driven storms, those with the high-time-resolution boundary condition were systematically better than those with the local-time-dependent (but lower-time-resolution) boundary condition. For the ICME-driven storms, those run sets employing the self-consistent electric field calculation were systematically better than those using the simplistic electric field. The implication, therefore, is that the inner magnetospheric physical response to strong driving is, at least to some degree, fundamentally different depending on the heliospheric structure impacting geospace. Specifically, for an accurate SYMH* comparison, it is found that CIR/HSS events respond strongly to transient spikes in the plasma outer boundary condition, while ICME passages exhibit a more highly structured electric field.

Citation: Liemohn, M. W., and R. Katus (2012), Is the storm time response of the inner magnetospheric hot ions universally similar or driver dependent?, *J. Geophys. Res.*, *117*, A00L03, doi:10.1029/2011JA017389.

1. Introduction

[2] *Liemohn et al.* [2010] conducted a systematic investigation of the similarities and differences in the inner magnetospheric hot ion response during different solar wind driving structures. In particular, they considered all of the intense storms (with a minimum Dst index [*Sugiura and Kamei*, 1991] of −100 nT or lower) during solar cycle 23 (from 1996 to 2005 inclusive), classifying them as driven by either an interplanetary coronal mass ejection (ICME) or a corotating interaction region and its trailing high-speed stream (CIR/HSS), as provided by *Zhang et al.* [2007a, 2007b]. They simulated all of these storms with the Hot Electron and Ion Drift Integrator (HEIDI) model using several different particle outer boundary conditions and electric field descriptions. Their data-model comparisons included Dst* (the component of the Dst index caused by near-Earth currents) from ground-based magnetometers and local-noon hot ion density and temperature measurements from geosynchronously orbiting satellites. For the Dst* comparisons, they focused on the peak of the storm, as was done by *Liemohn and Jazowski* [2008] for the initial HEIDI run set and analysis study. A finding of *Liemohn et al.* [2010] was that HEIDI consistently underpredicts the Dst* perturbation for CIR/HSS-driven storms while matching the dayside plasma observations relatively well, implying that there are other currents contributing to the low-latitude magnetic perturbations preferentially during CIR/HSS events compared to ICME events.

[3] An interesting point about the *Liemohn et al.* [2010] study is that it did not declare a best fit solution for the two solar structure storm sets. That is, the five simulation run sets each had strengths and weaknesses in the data-model comparisons, and the results were too similar across the run sets to quantitatively state which model configuration yielded the most accurate representation of the inner magnetosphere during those intervals.

[1]Atmospheric, Oceanic, and Space Sciences Department, University of Michigan, Ann Arbor, Michigan, USA.

0148-0227/12/2011JA017389

Table 1. Run Number Designations for the Combinations of Plasma and Electric Field Boundary Conditions

	LANL[a] Satellite Data	LANL[a] Reanalysis	Reanalysis Averages
Volland-Stern Electric Field	1	3	–
Self-Consistent Electric Field	2	4	5

[a]LANL, Los Alamos National Laboratory.

[4] Other studies, however, have clearly shown differences in the response of geospace to these two driving structures. *Tsurutani and Gonzalez* [1997] presented a detailed comparison of the ICME and CIR/HSS driven storm events, and *Borovsky and Denton* [2006] compiled an excellent summary of these similarities and differences in response to these two drivers. Inner magnetospheric simulations show that ICME-driven events are better simulated by drift physics models than are CIR/HSS events [e.g., *Jordanova*, 2006; *Jordanova et al.*, 2009], while global geospace models (that include a drift physics code for the inner magnetosphere) work fairly well for CIR/HSS storms [e.g., *Ilie et al.*, 2010]. Several studies have investigated the energy partitioning within geospace for these two types of events, finding that the relative percentage of energy dissipated in the auroral zone is much bigger for CIR/HSS storms than for ICME events [e.g., *Huttunen and Koskinen*, 2004; *Lu*, 2006; *Turner et al.*, 2006, 2009; *Pokhotelov et al.*, 2010]. Geosynchronous data has also been used to examine the different responses of these drivers, considering the keV energy range particle populations [e.g., *Denton et al.*, 2006; *MacDonald et al.*, 2010] and the more energetic electrons of the outer radiation belt [e.g., *Borovsky and Denton*, 2009; *Denton et al.*, 2010]. *Richardson et al.* [2006] provide a concise summary of intense geomagnetic storm dynamics during CIR/HSS events.

[5] Overall, it has been noted that these two styles of solar wind forcing are very different. Therefore, it is logical to ask the question: does the magnetosphere exhibit a fundamentally different response to the same forcing for these two types of drivers, or is the magnetospheric response fundamentally consistent between the two drivers and the difference in the typical response simply a matter of different typical forcing rates?

[6] This study addresses this question with a more detailed analysis of the simulation run sets from *Liemohn et al.* [2010]. Specifically, the entire storm interval is considered and compared against observations rather than just the storm peak, as was done in that study.

2. Numerical Approach

[7] This study builds on the numerical simulations initially presented by *Liemohn and Jazowski* [2008] and *Liemohn et al.* [2010]. In brief, the ion phase space density was calculated throughout near-Earth space by the Hot Ion and Electron Drift Integrator (HEIDI) model, a code originally written two decades ago [e.g., *Fok et al.*, 1993, 1995; *Jordanova et al.*, 1994, 1996]. HEIDI solves the gyration and bounce averaged kinetic equation for the phase space density of hot plasma species in the inner magnetosphere. HEIDI solves for each species on about 500 cells in physical space and about 3000 cells in velocity space at each of these spatial cell locations. The version used for this study [*Liemohn et al.*, 2004] includes either a specified electric field description or a self-consistently calculated electric field (for this study, the Kp-driven Volland-Stern model [*Volland*, 1973; *Stern*, 1975; *Maynard and Chen*, 1975]), based on the particle pressures and resulting field-aligned currents through the subauroral ionosphere [*Liemohn et al.*, 2001; *Ridley and Liemohn*, 2002]. It is coupled to the dynamic global core plasma model (DGCPM) of *Ober et al.* [1997] for the thermal plasmaspheric population, needed for Coulomb collisional scattering and decay. It also uses the *Rairden et al.* [1986] neutral hydrogen density model for the charge exchange collisional losses.

[8] The other important input to HEIDI is the outer boundary condition on the particle populations [e.g., *Thomsen et al.*, 1998]. For this study, three different boundary conditions are used. One set is the geosynchronous observations for the specific events, compiled into a single high-resolution time series (96 s cadence) and applied everywhere that there is inflow through the boundary. This time series is created from measurements from the magnetospheric plasma analyzer (MPA) [*Bame et al.*, 1993] and the synchronous orbiting particle analyzer (SOPA) [*Belian et al.*, 1992]. The second set is the *O'Brien and Lemon* [2007] reanalysis of the Los Alamos National Laboratory (LANL) MPA plasma density moments. This set provides local time as well as universal time variation, but only on an hourly cadence in both parameters. The third set is a nightside average of the O'Brien et al. reanalysis values (i.e., no local time variation and a 1 h universal time cadence). All three of these boundary conditions are modified with a compositional split specified by *Young et al.* [1982] and implemented by *Liemohn et al.* [1999]. The densities and temperatures from the three boundary conditions are very similar, on average.

[9] The five run sets considered for this study are defined in Table 1. There is only one run set with the third outer boundary condition because this run set was conducted as a test. It is expected that it would yield a result in between run sets 2 and 4.

[10] Simulations with the HEIDI model were conducted for a 4 day window around each of the 90 storm intervals from 1996 through 2005, yielding a database of 450 unique simulation results. Of the 90 intense storms, 11 are CIR/HSS events and 69 are ICME-driven disturbances, and 10 were excluded due to large data gaps (>4 h) in the LANL or solar wind inputs during the main phase. In addition, some simulations quit unexpectedly because of numerical stability conditions within HEIDI (i.e., the electric field became too large for the grid). The final usable simulation count is therefore 358, ranging from 66 to 80 for any given run set (see *Liemohn et al.* [2010] for more details on the number of usable storms for each run set). The Dst minimum time was always located within the second day of the simulation interval, providing at least 24 h of simulation prior to the peak and at least 48 h of simulation after it.

3. Results

[11] Data-model comparisons were conducted against the SYMH* time series. The SYMH* time series is defined for

this study like this [e.g., *Kozyra and Liemohn*, 2003; *Liemohn and Kozyra*, 2003]:

$$SYMH^* = \frac{SYMH - D_{MP} + D_Q}{C_{IC}}$$

where SYMH is the 1 min SYMH index compiled from low-latitude magnetometer stations by the Kyoto World Data Center, D_{MP} is an estimate of the contribution from the magnetopause currents (based on the upstream solar wind dynamic pressure [from *O'Brien and McPherron*, 2000]), D_Q is a quiet time offset value (11 nT) [also from *O'Brien and McPherron*, 2000], and C_{IC} is a correction factor for the contribution from induced currents within the Earth (here, 1.3) [e.g., *Langel and Estes*, 1985]. The solar wind values are from the OMNI database and are time lagged to the magnetopause using the minimum variance analysis front determination and propagation technique. A simulation equivalent to SYMH* comes from the Dessler-Parker-Sckopke relationship [*Dessler and Parker*, 1959; *Sckopke*, 1966],

$$SYMH^*_{DPS} = -3.98 \cdot 10^{-30} E_{RC}[\text{keV}]$$

(hereinafter referred to as $SYMH_{DPS}$), which relates the total energy content of the plasma within the inner magnetosphere, E_{RC}, to a magnetic perturbation at the center of the Earth. Both *Liemohn and Jazowski* [2008] and *Liemohn et al.* [2010] show example comparisons of observed versus modeled Dst* values for several storm intervals. Note that $SYMH_{DPS}$ is always a negative number, while the observed SYMH* can be positive, depending on SYMH and dynamic pressure at that time.

[12] Unlike the *Liemohn et al.* [2010] study, which only considered the comparison at the storm peak, the present study uses a 72 h window of comparison from each simulation. This window extends from 24 h prior to the Dst peak to 48 h after it. This interval was simulated for every storm event and therefore provides a consistent baseline for comparison between the events. *Ilie et al.* [2008] found that the average main phase for an intense storm is 12 h. A prepeak window of 24 h, therefore, will cover all of the main phase and, on average, an equal amount of prestorm quiet time. The recovery phase can last for many days after the peak, but is often (though not always) back up to less than 50% of the storm peak after 48 h [e.g., *Gonzalez et al.*, 1994; *Denton and Borovsky*, 2008]. This 72 h window, then, represents a comparison for the entirety of the disturbed interval for each storm event.

[13] Figure 1 shows superposed epoch time series of SYMH* for the CIR/HSS-driven storm events. The data for each storm has been referenced to the time of minimum Dst as listed by *Zhang et al.* [2007a, 2007b]. Figure 1a is the SYMH* time series, while Figures 1b–1f show the $SYMH_{DPS}$ time series for the five model run sets. For the calculation of SYMH* from SYMH, propagated solar wind data was used. When available, high-time-cadence (1 or 5 min) solar wind values were used, but if not, then 1 h values were interpolated to the SYMH time series. The color scale shows the number of values within 10 min by 10 nT bins. The solid white line is the mean of the SYMH* values and the dashed line is the median of the values. The time span of Figure 1 ranges from 24 h prior to the storm peak through 48 h after the storm peak. Note that some of the plots do not contain all 11 storms if, for some reason, that storm was excluded from the result analysis. Figure 1a has a slightly different *y* axis range for SYMH* than Figures 1b–1f have for the $SYMH_{DPS}$ values.

[14] It is seen in Figure 1 that the observed SYMH* time series has a wide spread in the main phase but tightens to a narrow cluster in the recovery phase. The model results all start with values just below zero; this is due to the quiet time initial condition imposed on the simulation (an empty domain for run sets 1 and 3, and one which has a $SYMH_{DPS}$ value of about −12 nT for the other run sets). Because these plots include 24 h prior to the storm peak, there is some prestorm quiet time included in the simulation results. Each of the model run sets then shows a systematic spreading in the $SYMH_{DPS}$ values near the storm peak and a realigning of the values late in the recovery phase.

[15] Figure 2 is a similar set of plots as Figure 1, but for the ICME-driven events. As in Figure 1, Figure 2a has a slightly different *y* axis range than do Figures 2b–2f. Careful examining of the solid and dashed lines in Figure 2 reveals that the mean is systematically offset (more negative) from the median. This is because of a skewing of the mean due to the few very large negative SYMH* values for some of the storms. Again, the model results all cluster just below zero at the start of the 72 h interval, spread out near the storm peak, and then refocus in the late recovery phase.

[16] Each of the modeled superposed epoch time series can be plotted against the corresponding observed SYMH* time series to yield a data-model comparison scatterplot. Specifically, the original 1 min resolution $SYMH_{DPS}$ results are paired with the corresponding SYMH* value for that minute. These scatterplots of the SYMH*-$SYMH_{DPS}$ comparisons for each of the five run sets are presented in Figures 3 and 4. All of the storms are overlaid in Figure 3 (the CIR/HSS drivers) and Figure 4 (the ICME drivers) for each of the five run sets. The color scale shows the number of data points within each 10 nT by 10 nT bin, and the solid diagonal line in each plot is a reference line with unity slope and zero offset, representing a perfect match between SYMH* and $SYMH_{DPS}$.

[17] The main feature of Figures 3a–3e is that nearly all of the storm time points are above the unity diagonal (the solid line in each plot), indicating that $SYMH_{DPS}$ time series from the HEIDI ion total energy content is underestimating the intensity of the magnetic perturbation recorded in SYMH* during CIR/HSS-driven storms. This is to be expected (for any HEIDI simulation) because the HEIDI code only extends to geosynchronous orbit, and there could be substantial current densities beyond this altitude [cf. *Turner et al.*, 2000, 2001; *Liemohn*, 2003; *Ganushkina et al.*, 2004, 2010; *Liemohn et al.*, 2011]. Another feature of Figure 3 is that the high-time-resolution (but no local-time-variation) boundary condition run sets (1 and 2) exhibit more scatter in the data-model comparison than do the run sets with the reanalysis outer boundary condition. Run sets 4 and 5 yield particularly narrow distributions of plots in $SYMH_{DPS}$ for a given SYMH*(although not aligned with a slope of one relative to SYMH*).

[18] In Figure 4, though, the results for the ICME-driven events are closer to the unity line. A bright patch of high

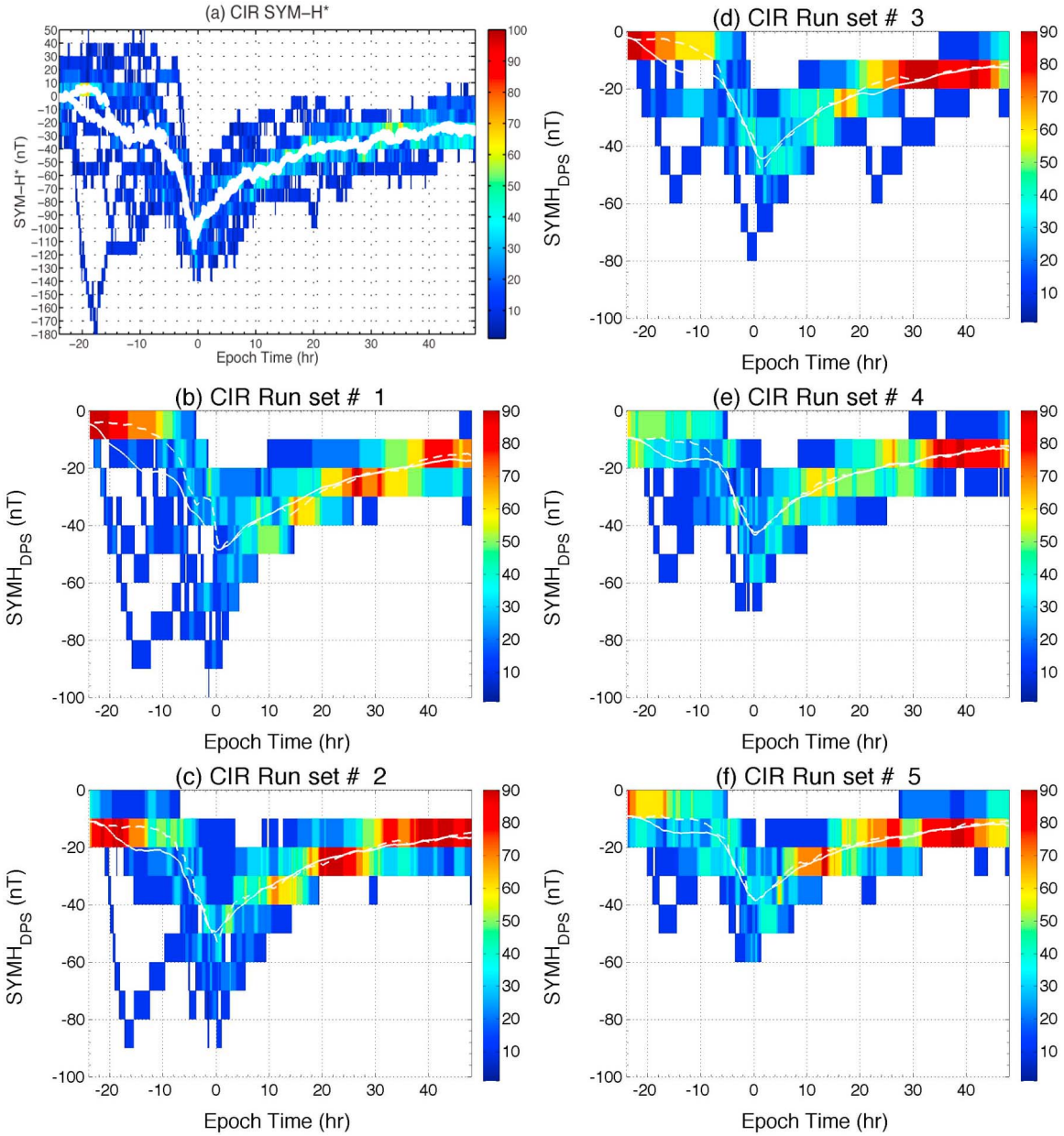

Figure 1. Superposed epoch times series of SYMH* for the CIR/HSS-driven storms calculated from (a) the observed values and (b–f) the five model run sets ($SYMH_{DPS}$), respectively. The color scale shows the number of values within each 10 min by 10 nT bin. The solid and dashed white lines are the mean and median, respectively. Note that Figure 1a has a different *y* axis scale than the others.

count rate per bin is seen in the upper right of each plot. This is partly due to the initial condition of the simulations producing a well-clustered set of simulation values in the prestorm interval, seen in Figure 2. A similar, although less pronounced, feature is seen in Figure 3 from the initial condition influence on the run set results in Figure 1. Qualitatively, there is more scatter in Figure 4 than in Figure 3, indicating that the resulting $SYMH_{DPS}$ values from HEIDI are more variable for ICME-driven storms than for CIR/HSS-driven storms. The observed SYMH* values for ICME-driven storms (Figure 4a) also exhibit greater scatter than those for CIR/HSS-driven storms (Figure 3a), indicating that this could be due to the differing storm size between the two solar wind driver structures.

[19] To quantify the goodness of fit within these scatterplots, statistical quantities such as the linear correlation coefficient (R) and the root-mean-square error (RMSE) can be calculated from the SYMH* and $SYMH_{DPS}$ values. As an additional quantification of the error in these statistics and the significance of the values between the various HEIDI run sets, a bootstrap method resampling was conducted [e.g., *Huber*, 1981; *Efron and Tibshirani*, 1993]. The bootstrap method has been used successfully before in space physics research to quantify the error on statistical results [e.g., *Reiff*,

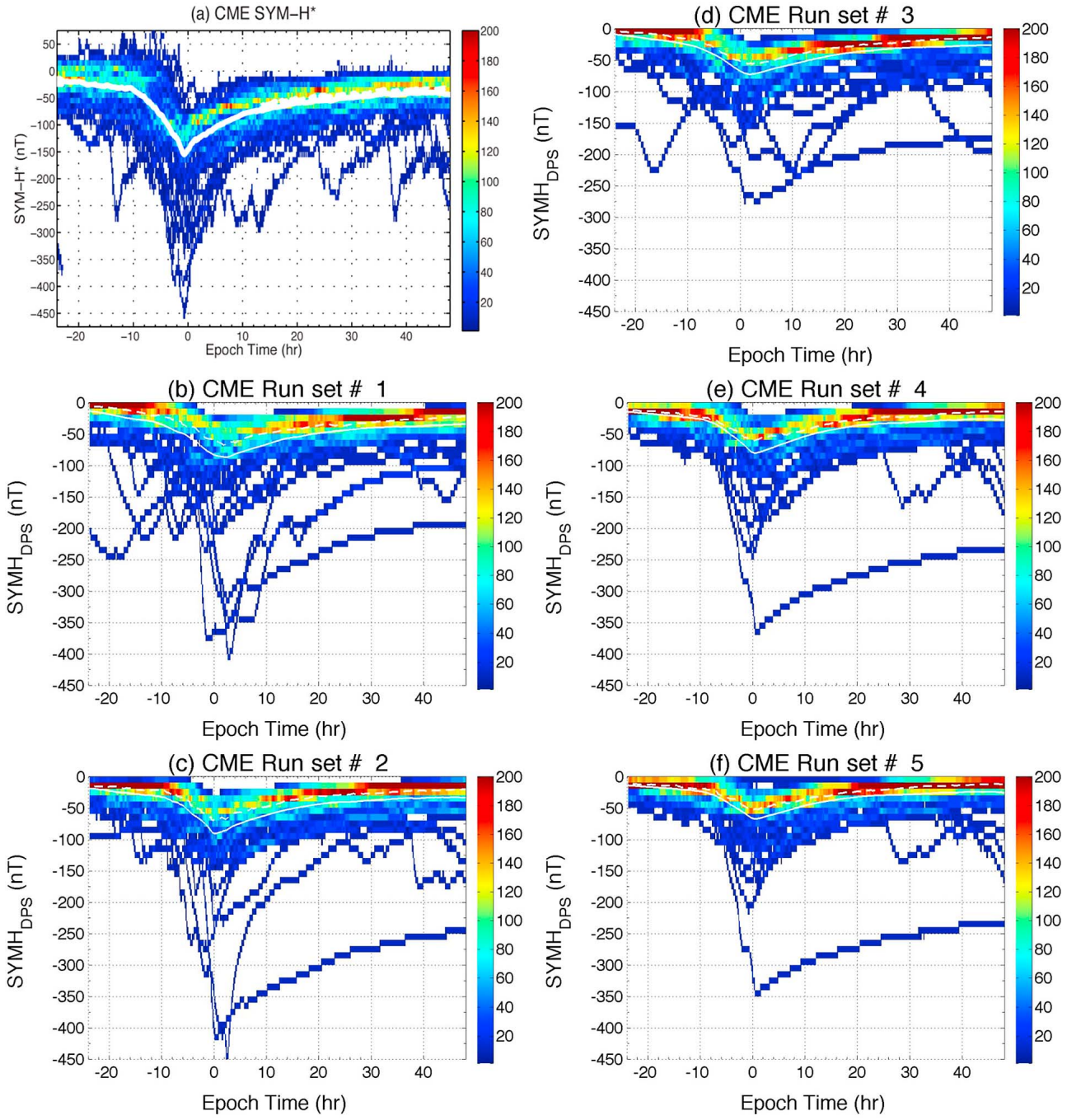

Figure 2. Superposed epoch times series of SYMH* for the ICME-driven storms calculated from (a) the observed values and (b–f) the five model run sets ($SYMH_{DPS}$), respectively. The color scale shows the number of values within each 10 min by 10 nT bin. The solid and dashed white lines are the mean and median, respectively.

1990; *Tsyganenko et al.*, 2003; *Green and Kivelson*, 2004; *Haraguchi et al.*, 2004], including for Dst data comparisons [*Jorgensen et al.*, 2004]. This is a technique in which a data set of *x*-*y* pairs of numbers (SYMH* and $SYMH_{DPS}$ values, in this case) is recreated as a new and slightly different data set. The new set is created by randomly choosing *x*-*y* pairs from the original data set (equal to the number of original pairs), but with the possibility of choosing the same pairs multiple times (at the expense of omitting other pairs). The statistics (R and RMSE) are then calculated for this new data set. This resampling procedure can be done many times to create a distribution of the statistics values, and a large number of resamplings reduces variation of the statistics. These distributions of R and RMSE have their own mean and standard deviation, and significance tests can be conducted between the R distribution for the various run sets to quantify if their correlations are different are not. In addition, the presence of nonnormal features in the original x or

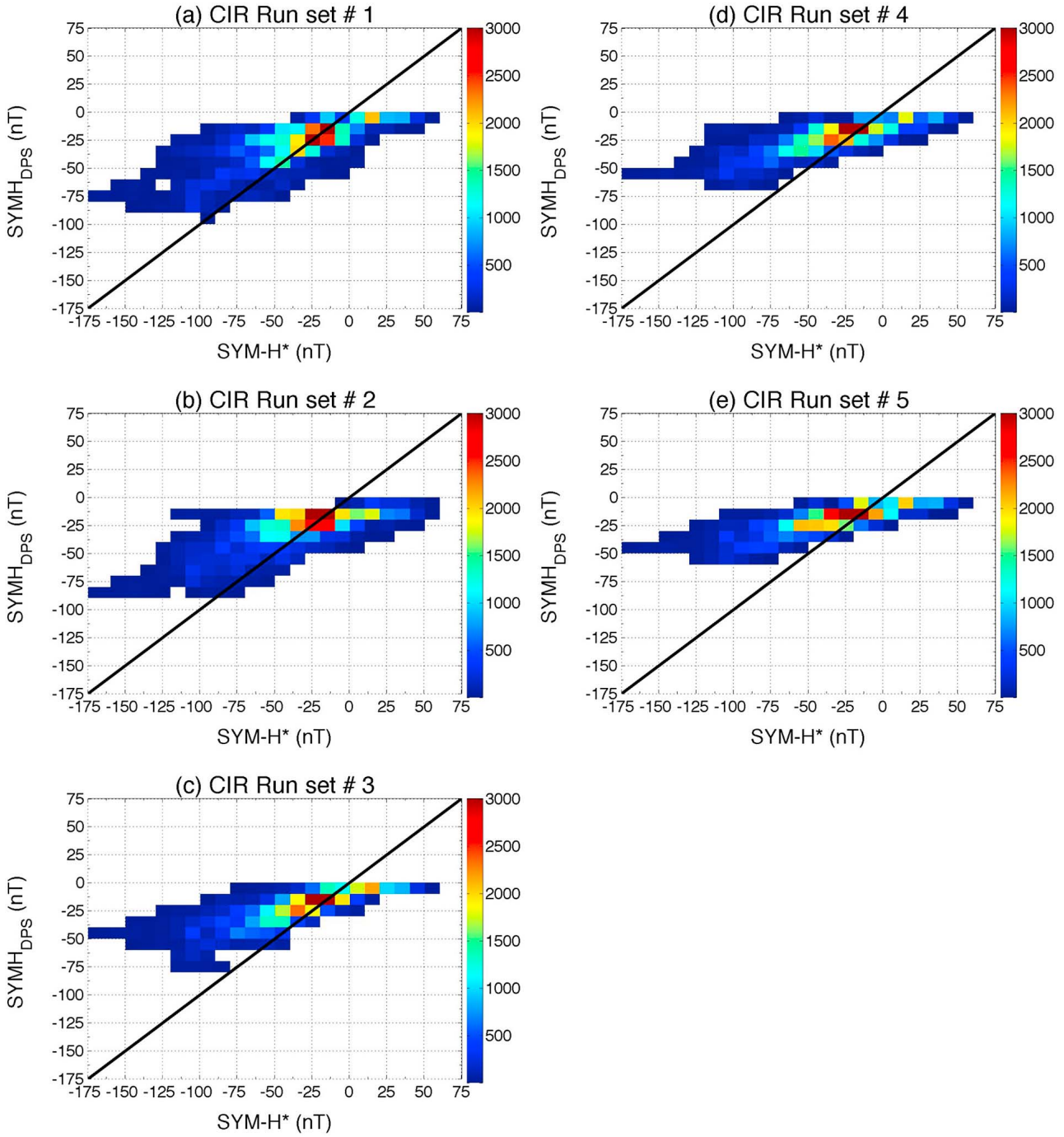

Figure 3. Scatterplots of the simulated $SYMH_{DPS}$ value against the observed SYMH* value for all storms for each of the five run sets for the CIR/HSS-driven storms. The color scale shows the number of points in each 10 nT by 10 nT bin. The diagonal solid line in each plot shows a perfect prediction.

y values might skew the mean or standard deviation in the resampled data, creating nonnormal features in the probability distribution (like a secondary peak or extended tail in one or both directions).

[20] Figure 5 shows the error statistic probability distributions found by applying the bootstrap method to SYMH* and $SYMH_{DPS}$. Shown are the correlation coefficient R (Figures 5a–5c) and the root-mean-square error (RMSE) (Figures 5d–5f) for the CIE/HSS-driven storms (Figures 5a and 5d) and the ICME-driven events (Figures 5b and 5e). The comparisons for the five HEIDI run sets are shown as the various colored lines. Various numbers of resamplings were tested, from 50 to 1000, stepping by increments of 50, to investigate the repeatability of the statistical results and the influence of the random number usage in the resampling method. It was found that at only 50 resamplings, the shape of the probability distributions varies a little between bootstrap analyses. However, for several

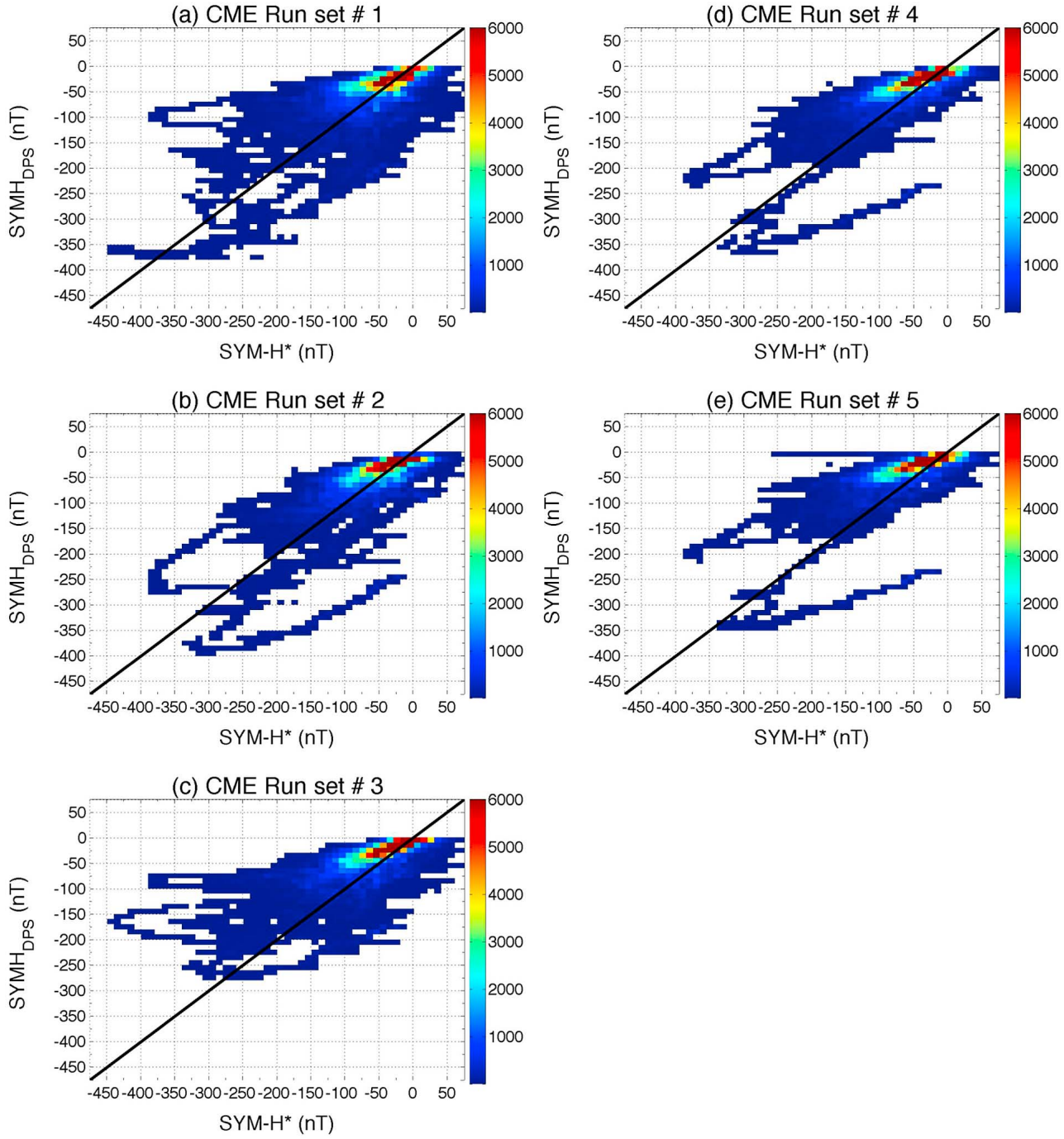

Figure 4. Scatterplots of the simulated $SYMH_{DPS}$ value against the observed SYMH* value for all storms for each of the five run sets for the ICME-driven storms. The color scale shows the number of points in each 10 nT by 10 nT bin. The diagonal solid line in each plot shows a perfect prediction.

hundred resamplings, the statistical results are identical from one bootstrap analysis to the next. In addition, the ordering of the run sets is the same for any of the resampling numbers that were tested, even down to only 50 resamplings. This confirms the statistical robustness findings of *Huber* [1981]. For these plots, 1000 bootstrap resamplings were conducted to construct the probability distributions.

[21] In the correlations (Figures 5a–5c), it is seen that the ordering of the five run sets is nearly identical for the two storm driver classifications. Run sets 3 and 4 are the best for both drivers, with run set 5 also being among the top for the CIR/HSS-driven events (Figure 5a). These run sets all use the LT-UT reanalysis outer boundary condition, but run set 3 has the Volland-Stern electric field while run sets 4 and 5 use a self-consistent field description. In addition, all of the correlations are slightly better for the CIR/HSS-driven storms than for the ICME-driven events (by a ΔR of about 0.15). The correlations for the various run sets usually do not

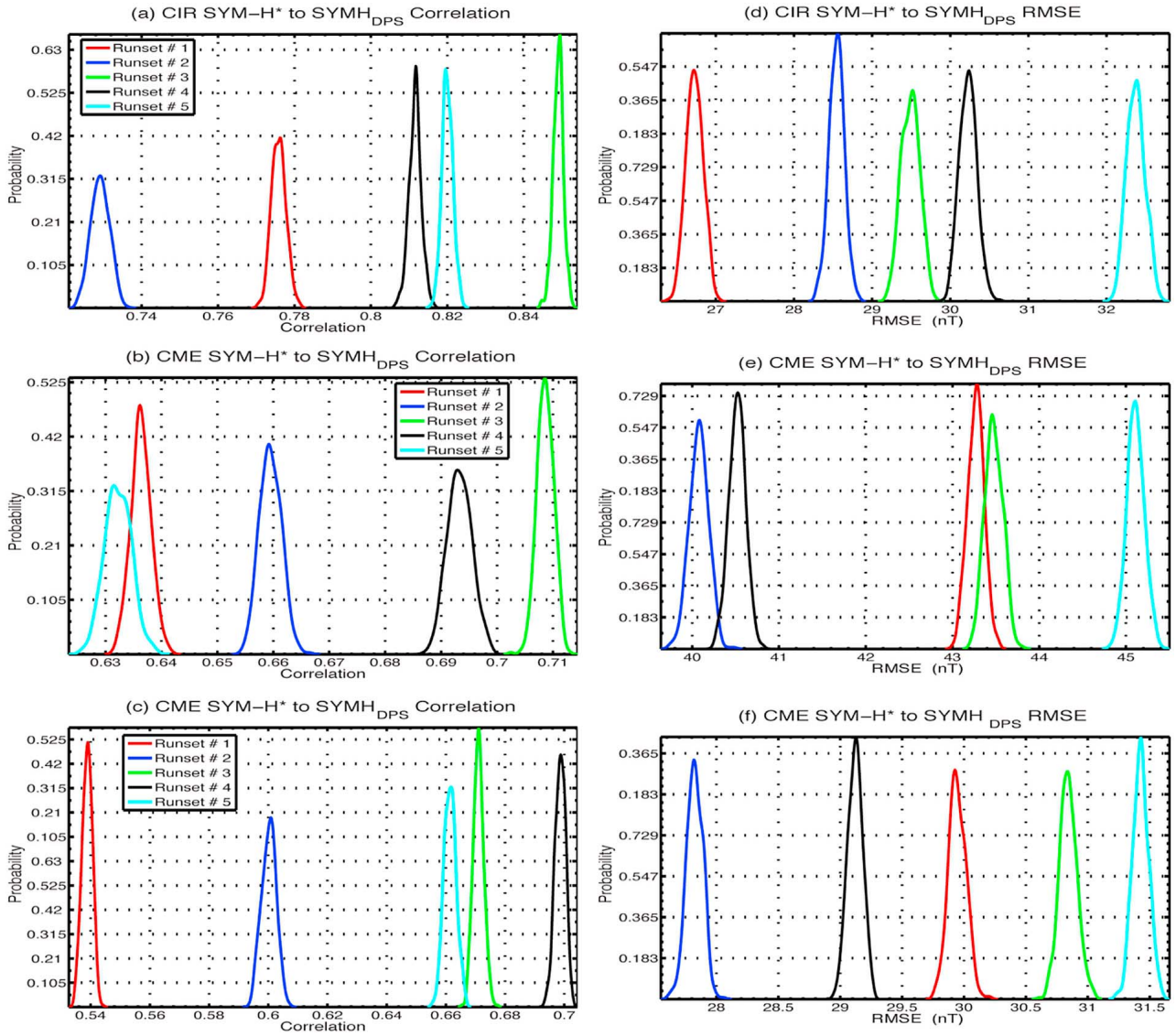

Figure 5. Probability distributions of correlation coefficients (left) and root-mean-square error (right) for (a, d) the CIR/HSS-driven storm intervals and (b, e) the ICME-driven events of the five run set $SYMH_{DPS}$ results against SYMH* (each colored line, as indicated in the legend). (c, f) Statistics for a subset of ICME events for the same intensity range as the CIR/HSS-driven storms. Note that each plot has a different *x* axis value set that does not start at zero.

overlap and significance tests indicate that they are all statistically different from each other when these distributions are visibly separated. The overlap of distributions can be used as a significance test, revealing the statistical significance of our conclusions about which run sets have a larger R or lower RMSE.

[22] For the RMSE distributions in Figures 5d–5f, the ordering of the HEIDI run sets is very different. Note that, for RMSE, a low value is better than a high one. Therefore, run sets 1, 2, and 3 are the best for the CIR/HSS storms while run sets 2 and 4 (Figure 5d) are the best for the ICME storms (Figure 5e). For the CIR/HSS-driven storms, two of the three best run sets based on RMSE are those with the high-time-resolution LANL boundary condition (but lacking local time variation), with the difference being the electric field description (Volland-Stern for run set 1 and self-consistent for run set 2). For the ICME-driven storms, the two best run sets both use the self-consistent electric field description, with the difference between them being the outer boundary condition for the hot ions (high-time-resolution LANL data for run set 2, LT-UT reanalyzed LANL data for run set 4).

[23] Basing conclusions from the comparisons of the intense CIR/HSS-driven events to the all of the intense ICME-driven events is not entirely appropriate because the range of storm sizes is different between these two drivers. A more proper comparison is with subset of the ICME-driven events that span the same intensity range as the CIR/HSS-driven events included in this study. This subset contains 34 of the original 69 usable ICME-driven storms. Statistics of this subset were conducted and the probability distributions for the R and RMSE parameters are shown in

Figures 5c and 5f, respectively. It is seen that the ordering of the run sets is nearly identical to the full ICME event list results of Figures 5b and 5e. The only difference is with the correlation coefficients, where the top two run sets (2 and 4) switched position and run set 5 advanced to third best.

[24] The shape of the probability distributions in Figure 5 is also a meaningful feature in the analysis. It reveals the closeness of the original SYMH* and $SYMH_{DPS}$ data sets to a normal distribution. If the shape of the probability distribution for a statistic is a nice Gaussian curve, then the original data from which the bootstrapping was taken is also a normal distribution. However, if there are secondary peaks in the probability distribution or some other non-Gaussian shape to the statistic, then this indicates that the original data was bimodal, skewed, or otherwise irregularly distributed. While there are a few small non-Gaussian features in the probability distributions, they are, for the most part, smooth and regularly shaped. Because these features are rare and subtle in Figure 5, they do not influence the findings of this study and further analysis of them is not needed.

4. Discussion

[25] To address the question of whether there is a fundamental difference in the inner magnetospheric response between CIR/HSS-driven storms and ICME-driven storms, we have considered 90 intense storm events from solar cycle 23 and simulated them with several numerical configurations of the HEIDI model. The results from these simulations were then compared against the SYMH* time series for each event. It is found that the best fit HEIDI run set changes depending on the goodness-of-fit statistic being considered. In addition, for a given statistic (R or RMSE), the best run set is sometimes the same between the two solar driver structures and sometimes very different, and the ordering of the run sets is usually very different between the two solar wind drivers.

[26] Based on these results, the short answer to the title question is, therefore, that the response is driver dependent. The inner magnetosphere is responding differently to solar wind driving and the physics of the response is fundamentally altered between these two heliospheric structures. This is a stronger conclusion than that of *Liemohn et al.* [2010], but this new study used the entirety of each storm interval instead of just the peak intensity of the storms. In addition, we have placed error estimates on the statistical goodness-of-fit quantifications, demonstrating that the differences between the run sets are often mathematically significant.

[27] The systematic differences between the storm driving structures for the two statistical parameters can be explained as follows. The correlation coefficients are a measure of how well a linear fit of $SYMH_{DPS}$ as a function of SYMH* reproduces the comparisons between these two values. This coefficient can be very high if the linear fit is good, but it does not guarantee a slope of unity and intercept of zero. That is, the two quantities might vary linearly with each other, but there could be a huge difference in the actual values, especially for largest negative SYMH*. Because the CIR/HSS-storm comparisons are clustered above the unity lines in Figure 3 while the ICME-storm comparisons are spread across a larger range of $SYMH_{DPS}$ values in Figure 4 (including many times with $SYMH_{DPS}$ less than SYMH*), the linear fit is systematically better for the CIR/HSS storms.

[28] The RMSE comparisons are a measure of how close the $SYMH_{DPS}$ values are to their corresponding SYMH* values, with a weighted error estimate that augments the contribution of large differences between these two quantities. For larger negative SYMH* values, the differences between the observed and modeled numbers can be substantially larger than the differences for small negative SYMH* values. That is, RMSE will systematically produce larger error values for larger storms. Because all of the CIR/HSS-driven storms have a SYMH minimum above −150 nT, this driving structure systematically produces smaller RMSE than the ICME-storm data-model comparisons.

[29] It is interesting to note that the ordering of the run sets for the ICME-driven events did not change when only the smaller intense storms were considered (comparing Figures 5b and 5e with Figures 5c and 5f). Time series plots like those in Figure 2 and scatterplots like those in Figure 4 were made for the subset of ICMEs (not shown), and they look very similar to those for the entire ICME intense storm list shown in Figures 2 and 4. This indicates that the magnetic storms driven by ICME solar wind structures are well represented by the settings of run sets 3 and 4 regardless of the intensity of SYMH*.

[30] The dependence of which run set is "best" on the statistical parameter being considered also can be explained. It is qualitatively seen in Figures 3 and 4 that the run sets with the reanalysis outer boundary condition values are more tightly clustered together. This is true for both of the driving structures. A closer examination of Figures 3 and 4 reveals that run sets 3–5 have systematically smaller (i.e., closer to zero) $SYMH_{DPS}$ values than those for run sets 1 and 2. This smaller intensity for the resulting storm is a result of the averaging conducted for the reanalysis, a step not done for the high-time-resolution boundary condition. Therefore, the outer boundary density can be significantly higher and more variable for run sets 1 and 2 compared to that from run sets 3–5. The influence of this clustering on the goodness-of-fit statistics is that the correlation coefficients are systematically higher for the reanalysis run sets. Therefore, run sets 3 and 4 (and even run set 5, for the CIR/HSS-driven storms) are the best for the correlation coefficient.

[31] The RMSE values are weighted to favor the larger differences between SYMH* and $SYMH_{DPS}$. That is, this error parameter is sensitive to the difference away from the unity lines in Figures 3 and 4. These larger differences systematically occur at larger negative values of SYMH*. Examining Figures 3 and 4 again, it is seen qualitatively that near the peaks of the storm intervals, certain run sets are grouped closer to the unity line than other run sets. For the CIR/HSS-driven storms, run sets 1 and 2 have more points closer to the unity line, in part because of the larger outer boundary density values and higher variability of these values. So, for this solar wind driver, the presence of transient spikes in the outer boundary condition were necessary for more accurate storm peak modeling.

[32] For the ICME-driven storms, all of the run sets are fairly close to the unity line, and therefore those with the tightest scattering yield the best RSME values, i.e., the run sets with the self-consistent electric fields. Therefore, for this solar wind driver, the RMSE values for the self-consistent

electric field run sets (2 and 4) are systematically lower than those for the simplistic empirical electric field model.

[33] What this implies is that the inner magnetosphere and near-Earth plasma sheet are responding in fundamentally different ways to the two solar wind driver structures, even for the same level of driving. The CIR/HSS-driven storms require transient spikes in the outer boundary condition for an accurate SYMH* comparison, while the ICME-driven events require the small-scale spatial and temporal structure of the self-consistent electric field to more accurately represent the SYMH* time series. The reason for this difference is still an unresolved question, but our conjecture about it that, because the driving is systematically stronger during ICME storms (see the statistics on this difference in the work of *Borovsky and Denton* [2006] and *Liemohn and Jazowski* [2008]), this forces the plasma sheet hot ions deeper into the inner magnetosphere, where the feedback of this hot ion pressure (via field-aligned current closure and the generation of these intense, small-scale flow patterns) is more pronounced.

5. Conclusions

[34] Five different model set up configurations of the HEIDI model were used to simulate all of the intense ($Dst_{min} < -100$ nT) magnetic storms from solar cycle 23 (from years 1996 through 2005). Two different electric field choices and three different outer boundary conditions for the hot ions were applied in different combinations. The storms were classified according to their heliospheric driving structure, and data-model comparisons were made against the SYMH* time series for each event. The question was posed regarding the nature of the physical response of the inner magnetosphere to these systematically different driving conditions.

[35] It was determined that the response was similar between the drivers when considering correlation coefficient, but are quite different when considering RMSE values. The scatterplots of these data-model comparisons confirm that the relationship systematically changes between the two solar wind structures. Therefore, it is concluded that the inner magnetosphere responds in a fundamentally different manner between CIR/HSS-driven storms and ICME-driven storms. Specifically, for an accurate SYMH* comparison, it is found that CIR/HSS events respond strongly to transient spikes in the plasma outer boundary condition while ICME passages exhibit a more highly structured electric field.

[36] An unexpected yet explainable outcome of these data-model comparisons is that the "best fit" run set is different for the two error estimates. For the correlation coefficient, the reanalysis outer boundary condition simulations were the best. For the root-mean-square error, the self-consistent electric field run sets yielded the lowest values for the ICME-driven storms and the high-time-resolution plasma input run sets were the best for the CIR/HSS-driven storms. This is because these two statistics are sensitive to different characteristics of the SYMH*-$SYMH_{DPS}$ relationship and to phases of the storm. If one is interested in predicting SYMH* variation throughout the time series, then the correlation coefficient is the better error estimate, as the linear relationship between SYMH* and $SYMH_{DPS}$ is a the quantity of relevance. However, a high correlation does not imply a slope of unity, and a model run set producing a tightly scattered data-model comparison will have a high correlation but is, nonetheless, systematically inaccurate. If one is focused on an accurate hot ion description near the peak of the storm, then the RMSE value is the better estimate. Run set 4, with the reanalysis plasma boundary condition and the self-consistent electric field, is common among the "best" run sets for most of the error measures for the two drivers, and therefore is a reasonable choice of model configuration for consistently accurate simulation results.

[37] **Acknowledgments.** The authors would like to thank NASA and NSF for funding this research through various grants, including a NASA Graduate Student Research Program fellowship from Marshall Space Flight Center. The authors would also like to thank Matt Jazowski for conducting the simulations being analyzed for this study; the Kyoto World Data Center for providing access to the Dst, SYMH, and Kp indices; and NASA's CDAWeb for providing access to the solar wind data. We would also like to thank the Los Alamos National Laboratory (LANL) and in particular Geoff Reeves, Mike Henderson, and Michelle Thomsen for making the LANL particle data available for the nightside boundary conditions.

[38] Masaki Fujimoto thanks the reviewers for their assistance in evaluating this paper.

References

Bame, S. J., D. J. McComas, M. F. Thomsen, B. L. Barraclough, R. C. Elphic, J. P. Glore, J. T. Gosling, J. C. Chavez, E. P. Evans, and F. J. Wymer, (1993), Magnetospheric plasma analyzer for spacecraft with constrained resources, *Rev. Sci. Instrum.*, *64*, 1026, doi:10.1063/1.1144173.

Belian, R. D., G. R. Gisler, T. Cayton, and R. Christensen (1992), High-*Z* energetic particles at geosynchronous orbit during the great solar proton event series of October 1989, *J. Geophys. Res.*, *97*, 16,897–16,906, doi:10.1029/92JA01139.

Borovsky, J. E., and M. H. Denton (2006), Differences between CME-driven storms and CIR-driven storms, *J. Geophys. Res.*, *111*, A07S08, doi:10.1029/2005JA011447.

Borovsky, J. E., and M. H. Denton (2009), Relativistic-electron dropouts and recovery: A superposed epoch study of the magnetosphere and the solar wind, *J. Geophys. Res.*, *114*, A02201, doi:10.1029/2008JA013128.

Denton, M. H., and J. E. Borovsky (2008), Superposed epoch analysis of high-speed stream effects at geosynchronous orbit: Hot plasma, cold plasma, and the solar wind, *J. Geophys. Res.*, *113*, A07216, doi:10.1029/2007JA012998.

Denton, M. H., J. E. Borovsky, R. M. Skoug, M. F. Thomsen, B. Lavraud, M. G. Henderson, R. L. McPherron, J. C. Zhang, and M. W. Liemohn (2006), Geomagnetic storms driven by ICME- and CIR-dominated solar wind, *J. Geophys. Res.*, *111*, A07S07, doi:10.1029/2005JA011436.

Denton, M. H., J. E. Borovsky, and T. E. Cayton (2010), A density-temperature description of the outer electron radiation belt during geomagnetic storms, *J. Geophys. Res.*, *115*, A01208, doi:10.1029/2009JA014183.

Dessler, A. J., and E. N. Parker (1959), Hydromagnetic theory of geomagnetic storms, *J. Geophys. Res.*, *64*, 2239–2252, doi:10.1029/JZ064i012p02239.

Efron, B., and R. J. Tibshirani (1993), *An Introduction to the Bootstrap*, 436pp., Chapman and Hall, New York.

Fok, M.-C., J. U. Kozyra, A. F. Nagy, C. E. Rasmussen, and G. V. Khazanov (1993), A decay model of equatorial ring current and the associated aeronomical consequences, *J. Geophys. Res.*, *98*, 19,381–19,393, doi:10.1029/93JA01848.

Fok, M.-C., T. E. Moore, J. U. Kozyra, G. C. Ho, and D. C. Hamilton (1995), Three-dimensional ring current decay model, *J. Geophys. Res.*, *100*, 9619–9632, doi:10.1029/94JA03029.

Ganushkina, N. Y., T. I. Pulkkinen, M. V. Kubyshkina, H. J. Singer, and C. T. Russell (2004), Long-term evolution of magnetospheric current systems during storms, *Ann. Geophys.*, *22*, 1317–1334, doi:10.5194/angeo-22-1317-2004.

Ganushkina, N., M. Liemohn, M. Kubyshkina, R. Ilie, and H. Singer (2010), Distortions of the magnetic field by storm-time current systems in Earth's magnetosphere, *Ann. Geophys.*, *28*, 123–140, doi:10.5194/angeo-28-123-2010.

Gonzalez, W. D., J. A. Joselyn, Y. Kamide, H. W. Kroehl, G. Rostoker, B. T. Tsurutani, and V. M. Vasyliunas (1994), What is a geomagnetic storm?, *J. Geophys. Res.*, *99*, 5771–5792, doi:10.1029/93JA02867.

Green, J. C., and M. G. Kivelson (2004), Relativistic electrons in the outer radiation belt: Differentiating between acceleration mechanisms, *J. Geophys. Res.*, *109*, A03213, doi:10.1029/2003JA010153.

Haraguchi, K., H. Kawano, K. Yumoto, S. Ohtani, T. Higuchi, and G. Ueno (2004), Ionospheric conductivity dependence of dayside region-0, 1, and

2 field-aligned current systems: Statistical study with DMSP-F7, *Ann. Geophys.*, *22*, 2775–2783, doi:10.5194/angeo-22-2775-2004.
Huber, P. J. (1981), *Robust Statistics*, 308pp., John Wiley, New York.
Huttunen, K. E. J., and H. E. J. Koskinen (2004), Importance of post-shock streams and sheath region as drivers of intense magnetospheric storms and high-latitude activity, *Ann. Geophys.*, *22*, 1729–1738, doi:10.5194/angeo-22-1729-2004.
Ilie, R., M. W. Liemohn, M. F. Thomsen, J. E. Borovsky, and J. Zhang (2008), The influence of epoch time selection on the results of superposed epoch analysis on ACE and MPA data, *J. Geophys. Res.*, *113*, A00A14, doi:10.1029/2008JA013241.
Ilie, R., M. W. Liemohn, J. U. Kozyra, and J. E. Borovsky (2010), An investigation of the magnetosphere–ionosphere response to real and idealized co-rotating interaction region events through global magnetohydrodynamic simulations, *Proc. R. Soc. A*, *466*(2123), 3279–3303, doi:10.1098/rspa.2010.0074.
Jordanova, V. K. (2006), Modeling the behavior of corotating interaction region driven storms in comparison with coronal mass ejection driven storms, in *Recurrent Magnetic Storms: Corotating Solar Wind Streams*, *Geophys. Monogr. Ser.*, vol. 167, edited by B. Tsurutani et al., pp. 77–84, AGU, Washington, D. C., doi:10.1029/167GM08.
Jordanova, V. K., J. U. Kozyra, G. V. Khazanov, A. F. Nagy, C. E. Rasmussen, and M.-C. Fok (1994), A bounce-averaged kinetic model of the ring current ion population, *Geophys. Res. Lett.*, *21*, 2785–2788, doi:10.1029/94GL02695.
Jordanova, V. K., L. M. Kistler, J. U. Kozyra, G. V. Khazanov, and A. F. Nagy (1996), Collisional losses of ring current ions, *J. Geophys. Res.*, *101*, 111–126, doi:10.1029/95JA02000.
Jordanova, V. K., H. Matsui, P. A. Puhl-Quinn, M. F. Thomsen, K. Mursula, and L. Holappa (2009), Ring current development during high speed streams, *J. Atmos. Sol. Terr. Phys.*, *71*, 1093–1102, doi:10.1016/j.jastp.2008.09.043.
Jorgensen, A. M., H. E. Spence, W. J. Hughes, and H. J. Singer (2004), A statistical study of the global structure of the ring current, *J. Geophys. Res.*, *109*, A12204, doi:10.1029/2003JA010090.
Kozyra, J. U., and M. W. Liemohn (2003), Ring current energy input and decay, *Space Sci. Rev.*, *109*, 105–131, doi:10.1023/B:SPAC.0000007516.10433.ad.
Langel, R. A., and R. H. Estes (1985), Large-scale, near-field magnetic fields from external sources and the corresponding induced magnetic field, *J. Geophys. Res.*, *90*, 2487–2494, doi:10.1029/JB090iB03p02487.
Liemohn, M. W. (2003), Yet another caveat to using the Dessler-Parker-Sckopke relation, *J. Geophys. Res.*, *108*(A6), 1251, doi:10.1029/2003JA009839.
Liemohn, M. W., and M. Jazowski (2008), Ring current simulations of the 90 intense storms during solar cycle 23, *J. Geophys. Res.*, *113*, A00A17, doi:10.1029/2008JA013466.
Liemohn, M. W., and J. U. Kozyra (2003), Lognormal form of the ring current energy content, *J. Atmos. Sol. Terr. Phys.*, *65*, 871–886, doi:10.1016/S1364-6826(03)00088-9.
Liemohn, M. W., J. U. Kozyra, V. K. Jordanova, G. V. Khazanov, M. F. Thomsen, and T. E. Cayton (1999), Analysis of early phase ring current recovery mechanisms during geomagnetic storms, *Geophys. Res. Lett.*, *26*, 2845–2848, doi:10.1029/1999GL900611.
Liemohn, M. W., J. U. Kozyra, C. R. Clauer, and A. J. Ridley (2001), Computational analysis of the near-Earth magnetospheric current system during two-phase decay storms, *J. Geophys. Res.*, *106*, 29,531–29,542, doi:10.1029/2001JA000045.
Liemohn, M. W., A. J. Ridley, D. L. Gallagher, D. M. Ober, and J. U. Kozyra (2004), Dependence of plasmaspheric morphology on the electric field description during the recovery phase of the 17 April 2002 magnetic storm, *J. Geophys. Res.*, *109*, A03209, doi:10.1029/2003JA010304.
Liemohn, M. W., M. Jazowski, J. U. Kozyra, N. Ganushkina, M. F. Thomsen, and J. E. Borovsky (2010), CIR versus CME drivers of the ring current during intense magnetic storms, *Proc. R. Soc. A*, *466*(2123), 3305–3328, doi:10.1098/rspa.2010.0075.
Liemohn, M. W., D. L. De Zeeuw, R. Ilie, and N. Y. Ganushkina (2011), Deciphering magnetospheric cross-field currents, *Geophys. Res. Lett.*, *38*, L20106, doi:10.1029/2011GL049611.
Lu, G. (2006), High-speed streams, coronal mass ejections, and interplanetary shocks: A comparative study of geoeffectiveness, in *Recurrent Magnetic Storms: Corotating Solar Wind Streams*, *Geophys. Monogr. Ser.*, vol. 167, edited by B. T. Tsurutani et al., pp. 97–111, AGU, Washington, D. C., doi:10.1029/167GM10.
MacDonald, E. A., L. W. Blum, S. P. Gary, M. F. Thomsen, and M. H. Denton (2010), High-speed stream driven inferences of global wave distributions at geosynchronous orbit: Relevance to radiation-belt dynamics, *Proc. R. Soc. A*, *466*(2123), 3351–3362, doi:10.1098/rspa.2010.0076.
Maynard, N. C., and A. J. Chen (1975), Isolated cold plasma regions: Observations and their relation to possible production mechanisms, *J. Geophys. Res.*, *80*, 1009–1013, doi:10.1029/JA080i007p01009.
O'Brien, T. P., and C. L. Lemon (2007), Reanalysis of plasma measurements at geosynchronous orbit, *Space Weather*, *5*, S03007, doi:10.1029/2006SW000279.
O'Brien, T. P., and R. L. McPherron (2000), An empirical phase space analysis of ring current dynamics: Solar wind control of injection and decay, *J. Geophys. Res.*, *105*, 7707–7719, doi:10.1029/1998JA000437.
Ober, D. M., J. L. Horwitz, and D. L. Gallagher (1997), Formation of density troughs embedded in the outer plasmasphere by subauroral ion drift events, *J. Geophys. Res.*, *102*, 14,595–14,602, doi:10.1029/97JA01046.
Pokhotelov, D., P. T. Jayachandran, C. N. Mitchell, and M. H. Denton (2010), High-latitude ionospheric response to co-rotating interaction region- and coronal mass ejection-driven geomagnetic storms revealed by GPS tomography and ionosondes, *Proc. R. Soc. A*, *466*(2123), 3391–3408, doi:10.1098/rspa.2010.0080.
Rairden, R. L., L. A. Frank, and J. D. Craven (1986), Geocoronal imaging with Dynamics Explorer, *J. Geophys. Res.*, *91*, 13,613–13,630, doi:10.1029/JA091iA12p13613.
Reiff, P. H. (1990), The use and misuse of statistics in space physics, *J. Geomagn. Geoelectr.*, *42*, 1145–1174, doi:10.5636/jgg.42.1145.
Richardson, I. G., et al. (2006), Major geomagnetic storms ($Dst \leq -100$ nT) generated by corotating interaction regions, *J. Geophys. Res.*, *111*, A07S09, doi:10.1029/2005JA011476.
Ridley, A. J., and M. W. Liemohn (2002), A model-derived storm time asymmetric ring current driven electric field description, *J. Geophys. Res.*, *107*(A8), 1151, doi:10.1029/2001JA000051.
Sckopke, N. (1966), A general relation between the energy of trapped particles and the disturbance field near the Earth, *J. Geophys. Res.*, *71*, 3125–3130.
Stern, D. P. (1975), The motion of a proton in the equatorial magnetosphere, *J. Geophys. Res.*, *80*, 595–599, doi:10.1029/JA080i004p00595.
Sugiura, M., and T. Kamei (1991), Equatorial Dst index 1957–1986, *IAGA Bull. 40*, ISGI Publ. Off., Saint-Maur-des-Fossés, France.
Thomsen, M. F., J. E. Borovsky, D. J. McComas, and M. R. Collier (1998), Variability of the ring current source population, *Geophys. Res. Lett.*, *25*, 3481–3484, doi:10.1029/98GL02633.
Tsurutani, B. T., and W. D. Gonzalez (1997), The interplanetary causes of magnetic storms: A review, in *Magnetic Storms*, *Geophys. Monogr. Ser.*, vol. 98, edited by B. T. Tsurutani et al., 77–89, AGU, Washington, D. C., doi:10.1029/GM098p0077.
Tsyganenko, N. A., H. J. Singer, and J. C. Kasper (2003), Storm-time distortion of the inner magnetosphere: How severe can it get?, *J. Geophys. Res.*, *108*(A5), 1209, doi:10.1029/2002JA009808.
Turner, N. E., D. N. Baker, T. I. Pulkkinen, and R. L. McPherron (2000), Evaluation of the tail current contribution to *Dst*, *J. Geophys. Res.*, *105*, 5431–5439, doi:10.1029/1999JA000248.
Turner, N. E., D. N. Baker, T. I. Pulkkinen, J. L. Roeder, J. F. Fennell, and V. K. Jordanova (2001), Energy content in the storm time ring current, *J. Geophys. Res.*, *106*, 19,149–19,156, doi:10.1029/2000JA003025.
Turner, N. E., E. J. Mitchell, D. J. Knipp, and B. A. Emery (2006), Energetics of magnetic storms driven by corotating interaction regions: A study of geoeffectiveness, in *Recurrent Magnetic Storms: Corotating Solar Wind Streams*, *Geophys. Monogr. Ser.*, vol. 167, edited by B. T. Tsurutani et al., pp. 113–124, AGU, Washington, D. C., doi:10.1029/167GM11.
Turner, N. E., W. D. Cramer, S. K. Earles, and B. A. Emery (2009), Geoefficiency and energy partitioning in CIR-driven and CME-driven storms, *J. Atmos. Sol. Terr. Phys.*, *71*, 1023–1031, doi:10.1016/j.jastp.2009.02.005.
Volland, H. (1973), A semiempirical model of large-scale magnetospheric electric fields, *J. Geophys. Res.*, *78*, 171–180, doi:10.1029/JA078i001p00171.
Young, D. T., H. Balsiger, and J. Geiss (1982), Correlations of magnetospheric ion composition with geomagnetic and solar activity, *J. Geophys. Res.*, *87*, 9077–9096, doi:10.1029/JA087iA11p09077.
Zhang, J., et al. (2007a), Solar and interplanetary sources of major geomagnetic storms ($Dst \leq -100$ nT) during 1996–2005, *J. Geophys. Res.*, *112*, A10102, doi:10.1029/2007JA012321.
Zhang, J., et al. (2007b), Correction to "Solar and interplanetary sources of major geomagnetic storms ($Dst \leq -100$ nT) during 1996–2005," *J. Geophys. Res.*, *112*, A12103, doi:10.1029/2007JA012891.

R. Katus and M. W. Liemohn, Atmospheric, Oceanic, and Space Sciences Department, University of Michigan, 2455 Hayward St., Ann Arbor, MI 48109-2143, USA. (liemohn@umich.edu)